

Ateneo de Manila University

Archium Ateneo

Environmental Science Faculty Publications

Environmental Science Department

4-24-2021

Enhanced Electrochemical Performances of Hollow-Structured N-Doped Carbon Derived from a Zeolitic Imidazole Framework (ZIF-8) Coated by Polydopamine as an Anode for Lithium-Ion Batteries

Da-Won Lee

Dong-A University

Achmad Yanuar Maulana

Dong-A University

Chaeun Lee

Dong-A University

Jungwook Song


Dong-A University

Cybelle M. Futralan

Ateneo de Manila University, cfutralan@ateneo.edu

Follow this and additional works at: <https://archium.ateneo.edu/es-faculty-pubs>

See next page for additional authors

 Part of the [Environmental Sciences Commons](#)

Custom Citation

Lee, D.-W., Maulana, A. Y., Lee, C., Song, J., Futralan, C. M., & Kim, J. (2021). Enhanced electrochemical performances of hollow-structured n-doped carbon derived from a zeolitic imidazole framework (ZIF-8) coated by polydopamine as an anode for lithium-ion batteries. *Energies*, 14(9), 2436. <https://doi.org/10.3390/en14092436>


This Article is brought to you for free and open access by the Environmental Science Department at Archium Ateneo. It has been accepted for inclusion in Environmental Science Faculty Publications by an authorized administrator of Archium Ateneo. For more information, please contact research@ateneo.edu.

Authors

Da-Won Lee, Achmad Yanuar Maulana, Chaeun Lee, Jungwook Song, Cybelle M. Futralan, and Jongsik Kim

Article

Enhanced Electrochemical Performances of Hollow-Structured N-Doped Carbon Derived from a Zeolitic Imidazole Framework (ZIF-8) Coated by Polydopamine as an Anode for Lithium-Ion Batteries

Da-Won Lee ^{1,2,†}, Achmad Yanuar Maulana ^{1,†} , Chaeun Lee ^{1,2}, Jungwook Song ^{1,2}, Cybelle M. Futralan ³ and Jongsik Kim ^{1,2,*}

¹ Department of Chemistry, Dong-A University, Busan 49315, Korea; 1607225@donga.ac.kr (D.-W.L.); 1776107@donga.ac.kr (A.Y.M.); chaeun817@donga.ac.kr (C.L.); jwsong@donga.ac.kr (J.S.)

² Department of Chemical Engineering (BK21 FOUR Graduate Program), Dong-A University, Busan 49315, Korea

³ Department of Environmental Science, Ateneo de Manila University, Quezon City 1108, Philippines; cfutralan@ateneo.edu

* Correspondence: jskimm@dau.ac.kr

† These authors contributed equally to this work.



Citation: Lee, D.-W.; Maulana, A.Y.; Lee, C.; Song, J.; Futralan, C.M.; Kim, J. Enhanced Electrochemical Performances of Hollow-Structured N-Doped Carbon Derived from a Zeolitic Imidazole Framework (ZIF-8) Coated by Polydopamine as an Anode for Lithium-Ion Batteries. *Energies* **2021**, *14*, 2436. <https://doi.org/10.3390/en14092436>

Academic Editor: Francesco Lufrano

Received: 14 March 2021

Accepted: 21 April 2021

Published: 24 April 2021

Publisher's Note: MDPI stays neutral with regard to jurisdictional claims in published maps and institutional affiliations.



Copyright: © 2021 by the authors. Licensee MDPI, Basel, Switzerland. This article is an open access article distributed under the terms and conditions of the Creative Commons Attribution (CC BY) license (<https://creativecommons.org/licenses/by/4.0/>).

Abstract: Doping heteroatoms such as nitrogen (N) and boron (B) into the framework of carbon materials is one of the most efficient methods to improve the electrical performance of carbon-based electrodes. In this study, N-doped carbon has been facily synthesized using a ZIF-8/polydopamine precursor. The polyhedral structure of ZIF-8 and the effective surface-coating capability of dopamine enabled the formation of N-doped carbon with a hollow structure. The ZIF-8 polyhedron served as a sacrificial template for hollow structures, and dopamine participated as a donor of the nitrogen element. When compared to ZIF-8-derived carbon, the HSNC electrode showed an improved reversible capacity of approximately 1398 mAh·g⁻¹ after 100 cycles, with excellent cycling retention at a voltage range of 0.01 to 3.0 V using a current density of 0.1 A·g⁻¹.

Keywords: Li-ion batteries; anode; N-doped carbon; Metal-Organic Frameworks (MOFs); hollow carbon structure

1. Introduction

The development of lithium-ion batteries (LIBs) is one of the most important achievements over the past three decades [1]. The success story of LIBs is reflected in their many applications in portable electronic devices and electric vehicles [2]. Since commercialization of LIBs, carbon materials have gained much attention [3]. At present, graphite has been used as a commercial anode material in LIBs due to its high stability and safety [4,5]. However, graphite cannot meet the demands required for high-performance LIBs, with a limited low storage capacity of about 372 mAh·g⁻¹ [6]. Therefore, numerous studies on carbon materials such as carbon nanotubes, nanospheres, hollow carbon structures, and graphene have been reported that focused mainly on the improvement of the energy density for LIBs by improving the conductivity and surface area of materials [7–10]. Among these studies, hollow carbon structures have received much attention due to their unique morphologies, which provide a shortened Li-ion diffusion length during cycling processes, and high reversible capacity and improved cycling stability with a discharge capacity of 421 mAh·g⁻¹ after 170 cycles at a current density of 1 A·g⁻¹ [9]. Furthermore, hollow carbon structures also can show remarkable properties in metallic lithium batteries due to the suppressed growth of dendrite [11].

Recently, carbon doped with various heteroatoms such as nitrogen (N), phosphorous (P), and boron (B) have been studied as anode materials to increase the electrochemical

properties of carbon [12–14]. Among the carbon anodes, N-doped carbon (NC) showed to be the most promising candidate due to the existence of two lone pair electrons on the nitrogen, which implied an improvement in its electronegativity and attractive interaction with charge carriers such as lithium ions. This would result in an enhanced storage capacity of LIBs [15]. The study of Ou et al. developed a nitrogen-rich porous carbon, which displayed a large discharge capacity of $1178 \text{ mAh}\cdot\text{g}^{-1}$ at the 100th cycle with a current density of $0.1 \text{ A}\cdot\text{g}^{-1}$ [16]. However, an additional synthetic step for incorporating nitrogen into the carbon matrix and an etching step with strong bases were required. Tian et al. also reported that the ratio of graphitic N to pyridinic N or pyrrolic N can be optimized on nitrogen-doped graphene sheets and would result in an increasing trend of the discharge capacity [17]. Nevertheless, the morphology of carbon particles (e.g., porosities) was not controlled. On the basis of these works, it is still very challenging to prepare N-doped carbon materials with high macro- and mesoporosities through a facile and mild synthetic method. Therefore, it will be meaningful to develop carbon-based anode materials with hollow morphologies and optimal composition of N-doped carbon species as an anode with high energy density in LIBs.

Metal–organic frameworks (MOFs) are the preferred precursors used to fabricate porous carbons because of their high thermal stability, low density, and high surface area [18–21]. Zeolitic imidazole frameworks (ZIF-8) have gained substantial attention in the development of NC materials [22,23]. However, NC derived from ZIF-8 exhibits a low degree of graphitization and numerous defects in the NC structure, which can cause poor electrical conductivity and limited electron transfer [24]. To solve this problem, several reports investigated the mixture of ZIF-8 precursors and secondary carbon sources such as carbon nanotubes and reduced graphene oxide (r-GO), and results showed an improvement in the electrical conductivity of NC [24,25]. Therefore, it is necessary to develop more appropriate strategies for the controllable synthesis of NC with a unique form, high surface area, and electrical conductivity.

In the present work, NC with a hollow structure was successfully synthesized by mixing ZIF-8 and dopamine. During this process, catechol and amine groups in dopamine would undergo self-polymerization to become polydopamine (PDA) under alkaline conditions and coat the ZIF-8 template (ZIF-8/PDA). After that, the mixture was carbonized using a tube furnace under argon (Ar) atmosphere. During the high-temperature carbonization process, ZIF-8 becomes a sacrifice template to form hollow-structured N-doped carbon (HSNC). A schematic of the HSNC synthesis route is illustrated in Figure 1. Based on the unique structure, the HSNC sample displayed a remarkable reversible capacity and high rate capability in LIB systems.

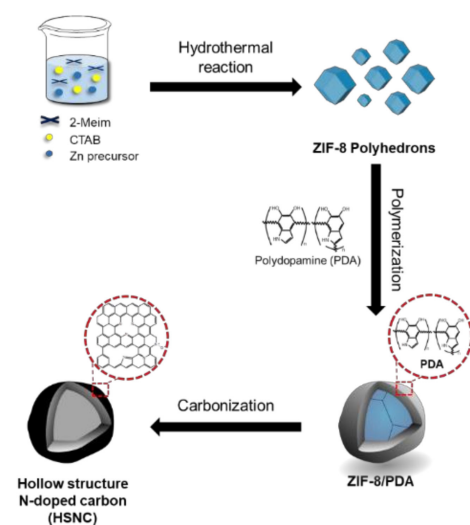


Figure 1. Preparation of the HSNC.

2. Materials and Methods

2.1. Sample Preparation

2.1.1. Preparation of ZIF-8 polyhedrons

About 0.1428 g of $\text{Zn}(\text{NO}_3)_2 \cdot 6\text{H}_2\text{O}$ and 2.1674 g of 2-methylimidazole were dissolved in 10 mL of deionized water in separate containers. Then, 2-methylimidazole solution was mixed with 1.44 mL of 0.01 M CTAB. Subsequently, the mixture was added to a $\text{Zn}(\text{NO}_3)_2 \cdot 6\text{H}_2\text{O}$ solution and stirred for 10 min until the color changed from clear to milky. The ZIF-8 polyhedron was produced by transferring that milky-colored solution into a 50 mL Teflon-lined autoclave to undergo hydrothermal reaction in an electric oven at 120 °C for 6 h. Lastly, samples were collected after drying in an oven at 80 °C overnight.

2.1.2. Synthesis of NC

The ZIF-8 polyhedron powder obtained after drying overnight was carbonized in a tube furnace at 900 °C for 3 h with a ramping rate of 5 °C min^{-1} under Ar gas flow (0.5 L min^{-1}).

2.1.3. Synthesis of HSNC

After the hydrothermal reaction, the ZIF-8 polyhedron solution was added in a drop-wise manner to 0.01 g of dopamine hydrochloride, which had been dissolved in 10 mL of distilled water. Then, the mixture was stirred for 6 h at room temperature to initiate the polymerization of dopamine on the surface of the ZIF-8 particles. The black precipitate was collected after filtration and washed several times with distilled water and ethanol. The ZIF-8/PDA powder was obtained after drying the precipitate in an oven at 80 °C overnight. Afterward, the ZIF-8/PDA powder was carbonized using similar conditions with the NC sample to produce the HSNC sample.

2.2. Characterization

2.2.1. Material Characterization

X-ray diffraction (XRD) patterns were recorded with a Rigaku model Miniflex 600 (Rigaku Co., Tokyo, Japan) X-ray diffractometer using $\text{Cu K}\alpha$ radiation at a wavelength of 1.5418 Å. The Raman spectra were measured using a He-Ne laser at a wavelength of 532 nm on an alpha300R (WITec, Ulm, Germany). The surface-element composition was measured by X-ray photoelectron spectroscopy (XPS, Theta Probe AR-XPS, Waltham, MA, USA). The pore volume and surface area of the samples were measured in a nitrogen environment using a gas adsorption analyzer (Micromeritics ASAP 2010, Unterschleissheim, Germany). The pore-size distribution was confirmed by the Barrett–Joyner–Halenda (BJH) method. The morphology and particle size were determined by transmission electron microscopy (TEM, JEOL JEM-2011, Tokyo, Japan) and scanning electron microscopy (SEM, JEOL JSM-6700F, Tokyo, Japan). Elemental mapping images were acquired with an energy dispersive X-ray spectrometer (EDX, JEOL JEM-2011, Tokyo, Japan).

2.2.2. Electrochemical Characterization

The electrodes were prepared by mixing the active material and PVDF binder with the solvent mixture of NMP (Aldrich; St. Louise, MO, USA) at a weight ratio of 9:1. The slurry was coated with a doctor-blade on Cu foil and dried at 80 °C for 30 min in a vacuum oven. The dried electrodes were obtained and cut into a circular shape with a diameter of 14 mm using a puncher with a loading density of 1.8 $\text{mg}\cdot\text{cm}^{-2}$. Then, samples were dried using a vacuum chamber at 80 °C for 2 h. Coin cells (2032) were assembled in an Ar-filled glove box using Celgard 2400 polypropylene membrane as a separation membrane and lithium metal as a reference electrode. In addition, 1 M LiPF_6 solution dissolved in an ethylene carbonate (EC): dimethyl carbonate (DMC) mixture was applied as electrolyte 1:1 *v/v*. Coin-cell performances were measured using a battery cycler (WonATech WBCS3000, Seoul, Korea) in the range of 0.01–3.0 V. The electrochemical impedance spectra (EIS) was measured using a ZIVE SP2 impedance analyzer (WonATech, Seoul, Korea). Electrochemical impedance measurements were obtained after charging at 3.0 V in the first cycle within the frequency

range of 10^{-2} – 10^5 Hz and amplitude of 10 mV AC signal. All electrochemical experiments were performed at 30 °C.

3. Results and Discussion

Figure 2a shows the XRD results of NC, HSNC, and their intermediate samples. The ZIF-8 polyhedron and ZIF-8/PDA samples showed a similar pattern to the simulated XRD of ZIF-8 and were indexed as a cubic structure with the $\bar{I}43m$ space group (JCPDS No. 62-1030) [26]. Results indicated that ZIF-8 was successfully synthesized, and PDA coating on the ZIF-8 particles did not change the structure of the ZIF-8 itself. Both the NC and HSNC samples also displayed two broad peaks at 23° and 43° that can be correlated to the (002) and (101) planes in the amorphous carbon structure [27]. From this, ZIF-8 served as a sacrifice template to produce polyhedron amorphous carbon and hollow amorphous carbon, respectively, during the carbonization process at high temperature. The lower angle of (002) peak of HSNC (23.3°) compared to NC (24.6°) and the broader peak of HSNC can be attributed to the increasing interlayer distance of d_{002} and more disordered carbon structure [28]. Using the Bragg equation, the interlayer of d_{002} for HSNC and NC samples was determined to be about 0.38 nm and 0.36 nm, respectively.

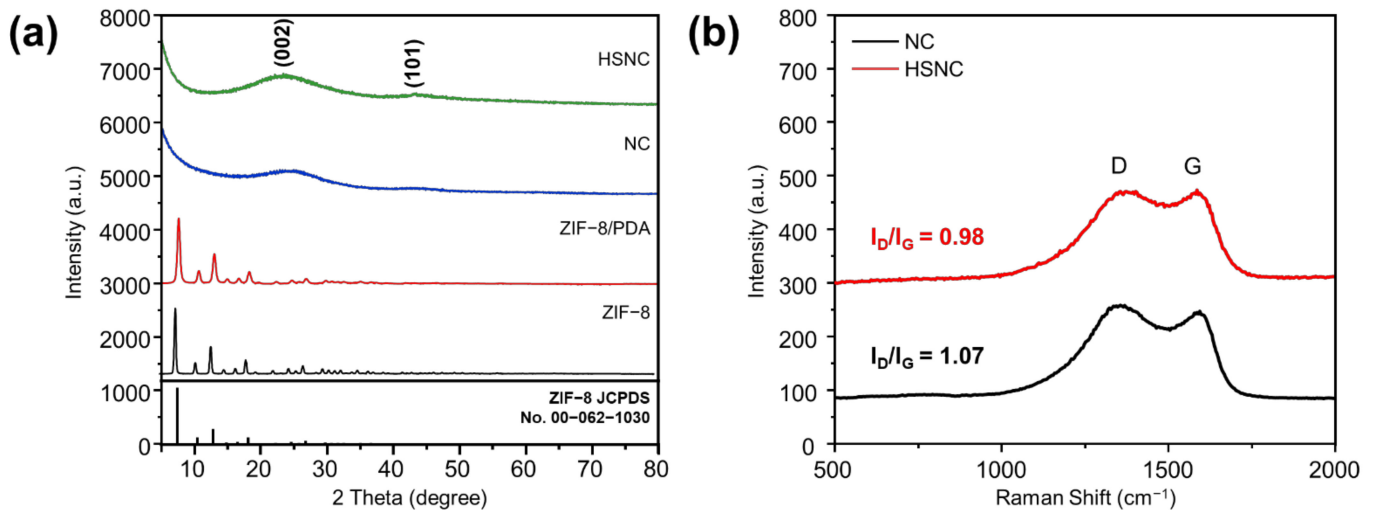


Figure 2. (a) XRD of ZIF-8/PDA, HSNC, and NC derived from ZIF-8; (b) Raman spectra of NC derived from ZIF-8 and HSNC.

Raman spectra shown in Figure 2b were carried out to understand the graphitization degree of the NC and HSNC samples. Both the NC and HSNC samples exhibited two broad peaks at 1350 and 1587 cm^{-1} that corresponded to the D and G bands, respectively [29]. The D band refers to the presence of defects and disorder in the carbon structure (sp^3), while the G band is identified as graphitic carbon structures (sp^2) [30]. A high I_D/I_G ratio generally indicates the generation of an increasing amount of defects and disorder in the carbon structure. The I_D/I_G values of the NC and HSNC samples were calculated to be 0.98 and 1.07, respectively. The higher amount of defects and disorder in the carbon structure of HSNC would imply easier transportation of charge carriers and electrolyte inside the structures, which is a favoring factor as an anode material in LIBs [15].

The value of I_D/I_G ratio can also be used to calculate the crystalline size (L_a) of carbon using the Tuinstra–Koenig relation (Equation (1)) [31]:

$$L_a \text{ (in nm)} = (2.4 \times 10^{-10}) \lambda^4 (I_D/I_G)^{-1} \quad (1)$$

where λ is the wavelength of the Raman light source (532 nm). The crystalline sizes of NC and HSNC were calculated to be 17.9 and 19.6 nm, respectively. Results showed that an increase in defects of the HSNC sample could lead to the swelling of the carbon structure.

The SEM and TEM images in Figure 3 were used to measure the morphologies and particle sizes of the NC and HSNC samples. The SEM image of NC in Figure 3a shows a polyhedron morphology with a particle size of 180–320 nm width and 170–380 nm length, indicating that the morphology of ZIF-8 was well maintained during the calcination process. The TEM images of the NC sample (Figure 3c) also show the solid structure of particles with sizes of 200–420 nm width and 220–400 nm length, which are well matched with SEM images. On the other hand, the HSNC sample (Figure 3d) was mainly composed of spherical and hollow-shaped nanoparticles with particle size of 160–370 nm width and 250–310 nm length. The morphological change to spherical shapes indicated that the PDA coating layers were homogeneously formed on the surface of the ZIF-8 polyhedron. The TEM images in Figure 3e,f show that the carbon particles of the HSNC sample had a unique hollow structure with a diameter of 120 nm and thickness of the outer carbon layers of about 20–40 nm. From the results, it is clear that the ZIF-8 was successfully decomposed as a sacrificial template. The hollow structure will be favorable for the effective diffusion of the electrolyte and a charge carrier such as lithium ions [32].

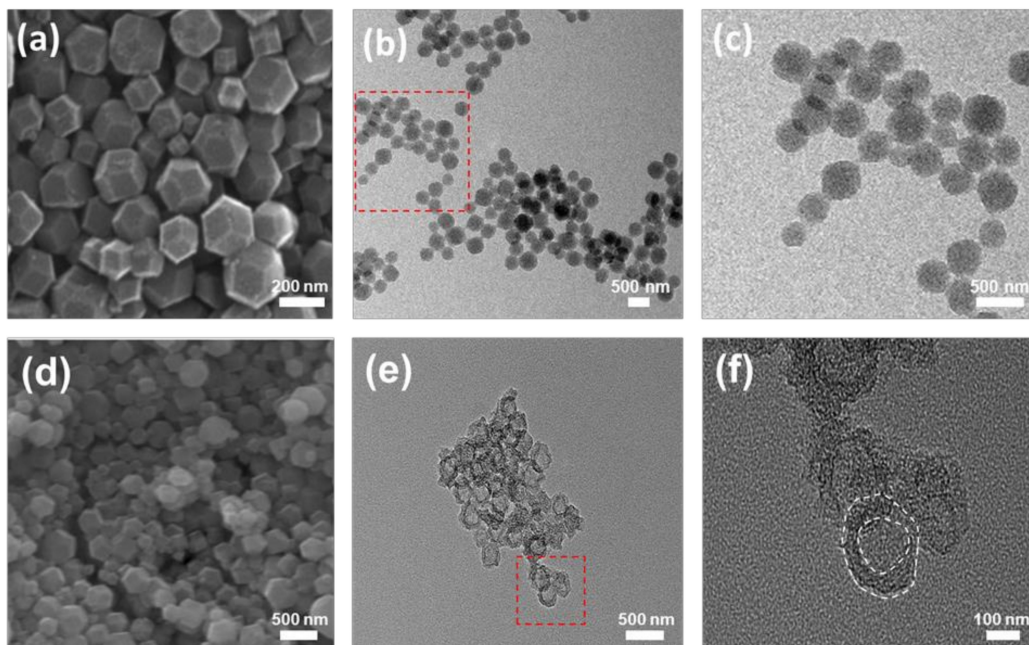


Figure 3. (a–c) SEM, TEM, and high-resolution TEM (HR-TEM) images of NC derived from ZIF-8, respectively; (d–f) SEM, TEM, HR-TEM images of HSNC, respectively. (The squared parts in (b) and (e) were magnified in (c) and (f), respectively).

The surface areas of the HSNC and NC samples were analyzed by BET analysis (Figure 4). The shape of the N_2 adsorption/desorption isotherm of both samples in Figure 4a clearly illustrates the IUPAC type IV curves, which can be correlated to the presence of a mesoporous structure [33]. Results were supported by the graph of the distribution of the pore sizes (Figure 4b), in which the presence of pore sizes within the range of 3.61–3.83 nm was observed. A higher pore volume of HSNC ($0.28 \text{ cm}^3 \cdot \text{g}^{-1}$) compared to NC ($0.16 \text{ cm}^3 \cdot \text{g}^{-1}$) was obtained, which could prove that there was a change in the morphology of the NC to the hollow structure. In consequence of these changes, the specific surface area of the HSNC sample was improved to about $437.96 \text{ m}^2 \cdot \text{g}^{-1}$, which was larger than the NC sample with a specific surface area of $394.65 \text{ m}^2 \cdot \text{g}^{-1}$. The improved surface area and pore volume of the HSNC compared to the NC sample corresponded to an increase in the active site of Li^+ ions. This resulted in an easier electrolyte penetration, which can significantly improve the electrochemical properties. In addition, Table S1 also shows that the HSNC sample had a competitive specific surface area compared to the other N-doped carbon-based anode materials, due to its unique morphologies.

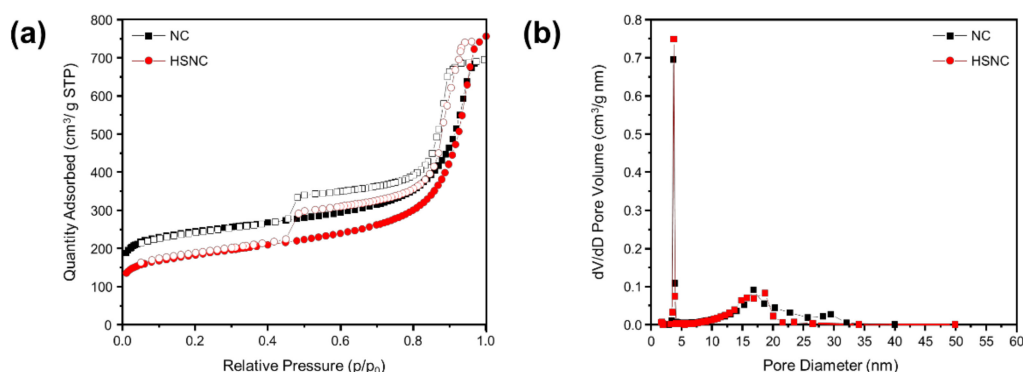


Figure 4. BET analysis showing the (a) nitrogen adsorption–desorption isotherms and (b) pore-size distribution of the HSNC and NC samples.

The surface chemical compositions of the HSNC and NC samples were analyzed using XPS experiments (Figure 5). The XPS spectra showed that HSNC and NC samples had similar patterns, which consisted of C, N, O, and Zn elements, as shown in Figure 5a. However, the HSNC sample showed slightly higher C and N peaks as a result of the presence of a PDA coating. In both samples, Zn2p peaks were observed, which indicated that a small amount of Zn still remained. However, considering that Zn is much more sensitive to X-ray sources than light atoms (C, N, O), the Zn content was traceable. In addition, many studies have reported that Zn doping can also be a conductivity-enhancing agent for anode materials, which might have helped to improve the electrochemical performance of the NC and HSNC samples [34]. Furthermore, the C1s region of the HSNC and NC samples in Figure 5b,c can be deconvoluted into four peaks that are specified as C=C (284.54 eV), C-O (286 eV), C=O (287.1 eV), and O-C=O (288.5 eV) [35,36]. The increasing ratio of C-O, C=O, and O-C=O bonds (29.24%) in the HSNC compared to that of the NC (26.43%) indicated more defects in the structure of the HSNC, which was attributable to the use of dopamine.

The N1s region of the HSNC and NC samples was fitted into four peaks at 398.2, 399.1, 400.6, and 403 eV, which corresponded to pyridinic N, pyrrolic N, graphitic N, and oxidized N, respectively (Figure 5d,e) [36,37]. The HSNC sample had a higher ratio of pyridinic and pyrrolic species (56.46%) than that of NC (51.12%). The pyridinic and pyrrolic N structures can be associated with the defects in the carbon structure. The presence of lone pairs of electrons in the pyridinic and pyrrolic N signified an improvement of the attractive interactions with Li ions [38]. From this, the superior electrochemical performances of HSNC due to the facilitated transportation of Li ions during cycling processes was predicted in LIBs.

The electrochemical performance of the HSNC and NC samples as anode materials for LIBs were investigated (Figure 6). The HSNC and NC samples displayed a similar galvanostatic discharge–charge graph (Figure 6a and Figure S1a). The first discharge cycle showed two plateaus at around 1.4–0.70 V and 0.5–0.01 V that were attributed to the formation of SEI layers and a lithiation reaction on the HSNC surface. These were consistent with the CV results shown in Figure 6b [39]. Notably, the CV curve during the first cycle showed two cathodic peaks. The cathodic peak at 0.68 V referred to the formation of SEI layer, while the cathodic peak at 0.01 V was correlated with the lithiation reaction [9]. In the subsequent cycles, the cathodic peak at 0.68 V disappeared, which indicated the presence of irreversible reactions during SEI layer formation in the first cycle. Meanwhile, the cathodic peak at 0.01 V and anodic peak at 0.37 V remained, which was related to the lithiation and delithiation reactions, respectively [9]. As mentioned above, the formation of an SEI layer is caused by side reactions between carbonate electrolyte and electrolyte salt [40]. The CV curve of the NC sample (Figure S1b) showed a similar pattern to that of the HSNC sample. However, a larger CV area of HSNC was observed when compared to the NC sample. This implies the HSNC sample had a superior cycling performance over the NC sample.

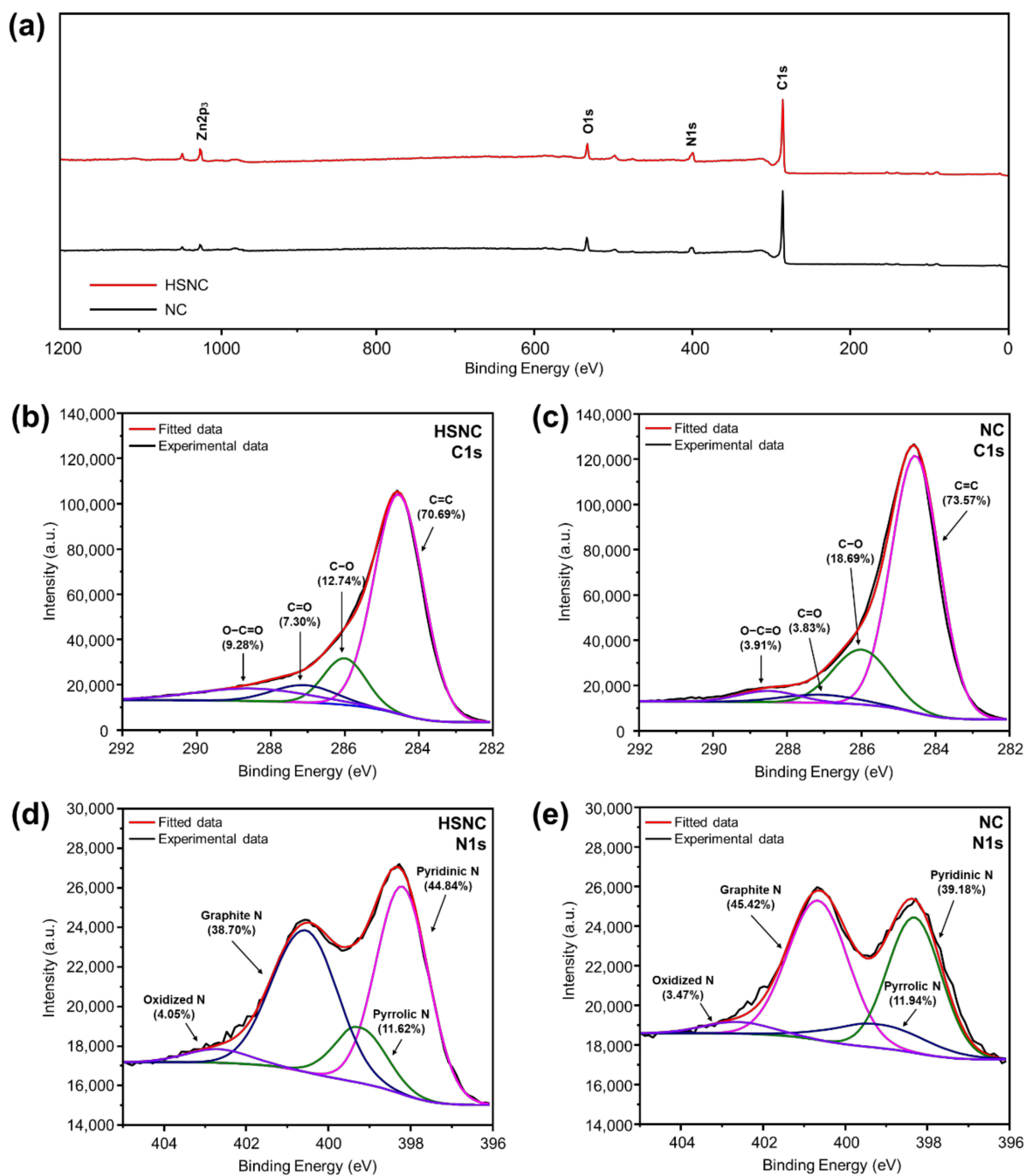


Figure 5. (a) XPS spectra of the HSNC and NC samples. C_{1s} region of (b) HSNC and (c) NC samples. N_{1s} regions of (d) HSNC and (e) NC samples.

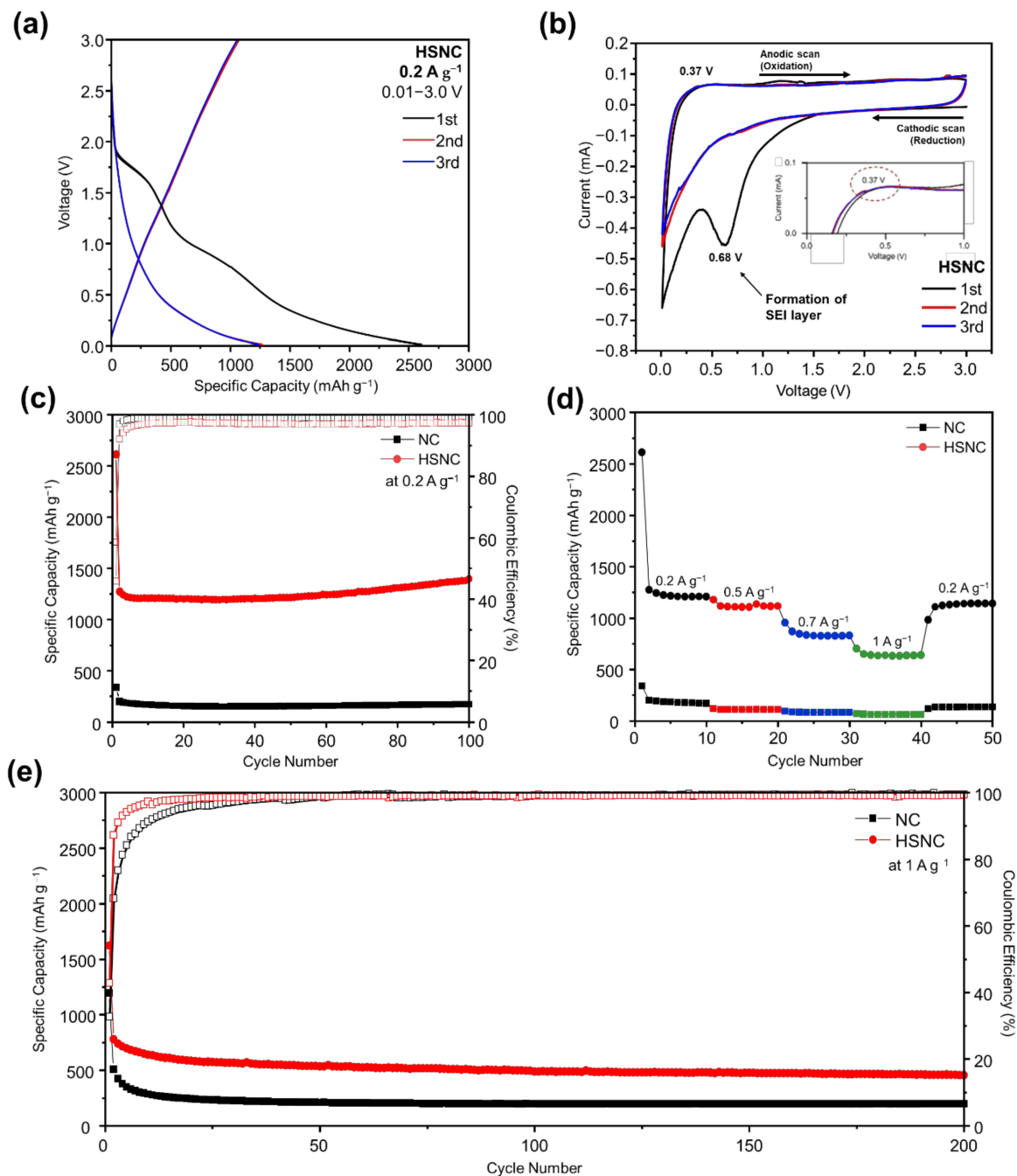


Figure 6. (a) Discharge–charge voltage profiles during the first three cycles at $0.2 \text{ A} \cdot \text{g}^{-1}$; (b) CV curve at a scan rate of $0.01 \text{ mV} \cdot \text{s}^{-1}$ from the HSNC sample in the voltage range of 0.01–3.0 V; (c) cycle performance at a current density of $0.2 \text{ A} \cdot \text{g}^{-1}$; (d) rate performance at various current densities; and (e) high rate-cycling performance at $1 \text{ A} \cdot \text{g}^{-1}$ for HSNC and NC.

Figure 6c shows the cycling performances of the NC and HSNC samples at a voltage range of 0.01–3.0 V and a current density of $0.2 \text{ A} \cdot \text{g}^{-1}$. The HSNC sample showed a high initial capacity of $2613.3 \text{ mAh} \cdot \text{g}^{-1}$, and the capacity decreased to $1273.5 \text{ mAh} \cdot \text{g}^{-1}$ in the second cycle. This reduction of capacity often occurs in anode materials because of the irreversible reaction of the SEI layer formation [41]. After the second cycle, the HSNC sample showed a stable retention that increased to $1398.3 \text{ mAh} \cdot \text{g}^{-1}$ at 100 cycles, which was almost four times higher than the theoretical capacity of graphite ($372 \text{ mAh} \cdot \text{g}^{-1}$). In comparison, the first discharge capacity of the NC sample only showed $337.6 \text{ mAh} \cdot \text{g}^{-1}$, and it decreased to $199.2 \text{ mAh} \cdot \text{g}^{-1}$ at the second cycle without increasing capacity. Finally, after 100 cycles, the discharge capacity of the NC sample only remained at $99.1 \text{ mAh} \cdot \text{g}^{-1}$.

The coulombic efficiencies (CEs) of the HSNC sample remained above 92% after the second cycle. The superior performance of the HSNC over the NC sample was mainly due to their higher defective carbon structure and hollow structures for the accessibility of more electrolytes, which improved the cyclability of the sample. The HSNC sample also presented the competitive cycling performance when compared to previous reports on N-doped carbon as anode materials in LIBs (Table S2).

The rate performance of the HSNC and NC samples at varying current densities that ranged from $0.2 \text{ A}\cdot\text{g}^{-1}$ to $1 \text{ A}\cdot\text{g}^{-1}$ were observed in Figure 6d. It can be clearly seen that the rate performance of the HSNC sample was better than that of the NC sample. In detail, the rate performance of the HSNC sample was determined to be 1404.1, 1179.0, 954.4, 702.9 $\text{mAh}\cdot\text{g}^{-1}$ at 0.2, 0.5, 0.7, and $1 \text{ A}\cdot\text{g}^{-1}$, respectively. When the current rate returned to $0.1 \text{ A}\cdot\text{g}^{-1}$, the HSNC sample still displayed an outstanding recovery rate of 87.5% when compared to the NC sample (80.1%). Moreover, the high rate performance of the HSNC sample at $1 \text{ A}\cdot\text{g}^{-1}$ showed a high reversible capacity of $455.7 \text{ mAh}\cdot\text{g}^{-1}$ after 200 cycles, with an outstanding fading rate of 0.002% when compared to NC sample (Figure 6e).

Figure 7 shows the EIS measurement of the HSNC and NC samples after 100 cycles with a current density of $0.2 \text{ A}\cdot\text{g}^{-1}$. The Nyquist plots of the HSNC and NC samples in Figure 7a are composed of a semicircle and sloped line, which were associated with the charge-transfer resistance (R_{ct}) and Warburg resistance (W_o) for the diffusion of Li^+ ions, respectively [42]. After fitting with an equivalent circuit, the simulated data were obtained (Table S3). Results showed that the R_{ct} values of the HSNC (115.54Ω) were smaller than those of the NC (505.81Ω), which indicated the good charge-transfer ability of HSNC.

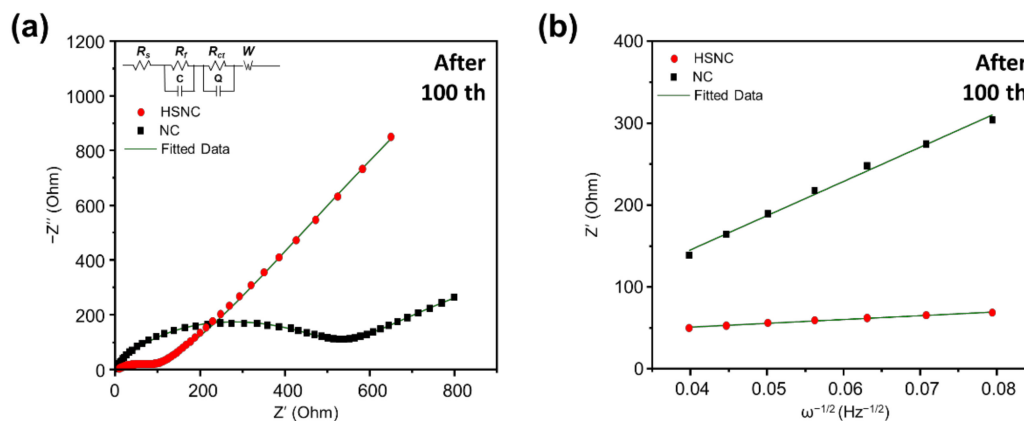


Figure 7. (a) Nyquist plots and (b) relationships between Z'_{real} and $\omega^{-1/2}$ at a low-frequency region of the HSNC and NC samples after 100 cycles at a current density of $0.2 \text{ A}\cdot\text{g}^{-1}$ and a voltage range of 0.01–3.0 V.

Moreover, the plot of the W_o sloped region as Z'_{real} vs $\omega^{-1/2}$ in Figure 7b can be used to estimate the diffusion coefficient of Li^+ ions (D_{Li^+}) using the equations shown below:

$$Z'_{\text{real}} = R_s + R_{ct} + \sigma_{\omega} \omega^{-1/2} \quad (2)$$

$$D_{\text{Li}^+} = 0.5 \left(\frac{RT}{An^2F^2C} \right)^2 \quad (3)$$

where R is the gas constant, T is the absolute temperature (K), A is the surface area of the electrode, n is the number of electrons related to the redox reaction, F is the Faraday constant, σ_{ω} is the Warburg coefficient, and C is the concentration of lithium ions.

The diffusion coefficient of lithium ions (D_{Li^+}) of the HSNC and NC samples were calculated to be 3.15×10^{-17} and $4 \times 10^{-19} \text{ cm s}^{-1}$, respectively. Overall, results showed that the unique hollow morphologies and the presence of defects in the HSNC structure led to the enhancement of the electrode kinetics reaction and resistance for the redox reactions with lithium ions when compared to NC sample.

4. Conclusions

In this study, hollow N-doped carbon was designed and fabricated through facile carbonization of ZIF-8 coated by PDA. The ZIF-8 polyhedron successfully acted as a sacrificial template during the carbonization step to form the hollow structure in the HSNC sample. In addition, 2-methylimidazole and dopamine served as carbon and nitrogen sources. The hollow structure of the HSNC sample resulted in higher surface area and pore volume compared to the NC sample, enabling the accelerated transportation of charge carriers and electrolyte inside the electrode structure. This unique hollow structure might be a key factor for the improved electrochemical performance of the HSNC sample. Moreover, the HSNC had the higher contents of pyridine and pyrrolic functional groups compared to NC sample, which was favorable to attract Li ions during cycling processes due to their lone pair electrons and defect configurations in the carbon structure. Because of these features, the HSNC sample exhibited an outstanding reversible capacities and excellent cycling stability as an anode material for LIBs compared to the NC sample. Furthermore, HSNC with a high surface area and nitrogen content, macro- and mesoporous pores, and a hollow structure can be utilized in various applications beyond batteries; for example, in adsorbents, catalysis, fuel cells, and supercapacitors.

Supplementary Materials: The following are available online at <https://www.mdpi.com/article/10.3390/en14092436/s1>, Figure S1: (a) Discharge–charge voltage profiles of the first three cycles at 0.2 A g⁻¹, and (b) CV curve at a scan rate of 0.1 mV s⁻¹ from NC sample in the voltage range of 0.01–3.0 V; Table S1: The various BET surface area data of N-doped carbon materials for LIBs; Table S2: The various cycling performances of N-doped carbon materials for LIBs; Table S3: The fitting parameters for EIS spectra of the NC and HSNC samples in LIBs.

Author Contributions: Conceptualization, J.K.; investigation, data collection, and analysis, D.-W.L., A.Y.M., C.L., and J.S.; writing—original draft preparation, D.-W.L. and A.Y.M.; writing—review and editing, C.M.F. and J.K.; supervision, project administration, and funding acquisition, J.K. All authors have read and agreed to the published version of the manuscript.

Funding: This research was funded by the Basic Science Research Program through the National Research Foundation of Korea (NRF), which is funded by the Ministry of Education (2016R1A6A1A03012812).

Institutional Review Board Statement: Not applicable.

Informed Consent Statement: Not applicable.

Data Availability Statement: All data generated by this study are contained within the article and the attached supplementary materials.

Acknowledgments: We would like to acknowledge the grant from NRF (2016R1A6A1A03012812).

Conflicts of Interest: The authors declare no conflict of interest.

References

1. Manthiram, A. A reflection on lithium-ion battery cathode chemistry. *Nat. Commun.* **2020**, *11*, 1–9. [[CrossRef](#)]
2. Zhang, H.; Li, C.; Eshetu, G.G.; Laruelle, S.; Grugeon, S.; Zanghi, K.; Julien, C.; Mauger, A.; Guyomard, D.; Rojo, T.; et al. From Solid-Solution Electrodes and the Rocking-Chair Concept to Today's Batteries. *Angew. Chem.* **2020**, *132*, 542–546. [[CrossRef](#)]
3. Luo, J.-M.; Sun, Y.-G.; Guo, S.-J.; Xu, Y.-S.; Chang, B.-B.; Liu, C.-T.; Cao, A.-M.; Wan, L.-J. Hollow carbon nanospheres: Syntheses and applications for post lithium-ion batteries. *Mater. Chem. Front.* **2020**, *4*, 2283–2306. [[CrossRef](#)]
4. Qin, L.; Zhang, S.; Zheng, J.; Lei, Y.; Zhai, D.; Wu, Y. Pursuing graphite-based K-ion O₂ batteries: A lesson from Li-ion batteries. *Energy Environ. Sci.* **2020**, *13*, 3656–3662. [[CrossRef](#)]
5. Li, X.; Sun, X.; Hu, X.; Fan, F.; Cai, S.; Zheng, C.; Stucky, G.D. Review on comprehending and enhancing the initial Coulombic efficiency of anode materials in lithium-ion/sodium-ion batteries. *Nano Energy* **2020**, *77*, 105143. [[CrossRef](#)]
6. Yang, C.; Zhang, X.; Li, J.; Ma, J.; Xu, L.; Yang, J.; Liu, S.; Fang, S.; Li, Y.; Sun, X.; et al. Holey graphite: A promising anode material with ultrahigh storage for lithium-ion battery. *Electrochim. Acta* **2020**, *346*, 136244. [[CrossRef](#)]
7. Landi, B.J.; Ganter, M.J.; Cress, C.D.; Dileo, R.A.; Raffaele, R.P. Carbon nanotubes for lithium ion batteries. *Energy Environ. Sci.* **2009**, *2*, 638–654. [[CrossRef](#)]
8. Xiao, J.; Yao, M.; Zhu, K.; Zhang, D.; Zhao, S.; Lu, S.; Liu, B.; Cui, W.; Liu, B. Facile synthesis of hydrogenated carbon nanospheres with a graphite-like ordered carbon structure. *Nanoscale* **2013**, *5*, 11306–11312. [[CrossRef](#)] [[PubMed](#)]

9. Li, P.; Liu, J.; Wang, Y.; Liu, Y.; Wang, X.; Nam, K.-W.; Kang, Y.-M.; Wu, M.; Qiu, J. Synthesis of ultrathin hollow carbon shell from petroleum asphalt for high-performance anode material in lithium-ion batteries. *Chem. Eng. J.* **2016**, *286*, 632–639. [[CrossRef](#)]
10. Su, Y.; Li, S.; Wu, D.; Zhang, F.; Liang, H.; Gao, P.; Cheng, C.; Feng, X. Two-Dimensional Carbon-Coated Graphene/Metal Oxide Hybrids for Enhanced Lithium Storage. *ACS Nano* **2012**, *6*, 8349–8356. [[CrossRef](#)]
11. Liu, Y.; Zhen, Y.; Li, T.; Bettels, F.; He, T.; Peng, M.; Liang, Y.; Ding, F.; Zhang, L. High-Capacity, Dendrite-Free, and Ultrahigh-Rate Lithium-Metal Anodes Based on Monodisperse N-Doped Hollow Carbon Nanospheres. *Small* **2020**, *16*, 2004770. [[CrossRef](#)]
12. Way, B.; Dahn, J. The effect of boron substitution in carbon on the intercalation of lithium in $\text{Li}_x(\text{Bz C}1-z)_6$. *J. Electrochem. Soc.* **1994**, *141*, 907. [[CrossRef](#)]
13. Li, Z.; Xu, Z.; Tan, X.; Wang, H.; Holt, C.M.; Stephenson, T.; Olsen, B.C.; Mitlin, D. Mesoporous nitrogen-rich carbons derived from protein for ultra-high capacity battery anodes and supercapacitors. *Energy Environ. Sci.* **2013**, *6*, 871–878. [[CrossRef](#)]
14. Zhang, C.; Mahmood, N.; Yin, H.; Liu, F.; Hou, Y. Synthesis of Phosphorus-Doped Graphene and its Multifunctional Applications for Oxygen Reduction Reaction and Lithium Ion Batteries. *Adv. Mater.* **2013**, *25*, 4932–4937. [[CrossRef](#)] [[PubMed](#)]
15. Wu, J.; Pan, Z.; Zhang, Y.; Wang, B.; Peng, H. The recent progress of nitrogen-doped carbon nanomaterials for electrochemical batteries. *J. Mater. Chem. A* **2018**, *6*, 12932–12944. [[CrossRef](#)]
16. Ou, J.; Zhang, Y.; Chen, L.; Zhao, Q.; Meng, Y.; Guo, Y.; Xiao, D. Nitrogen-rich porous carbon derived from biomass as a high performance anode material for lithium ion batteries. *J. Mater. Chem. A* **2015**, *3*, 6534–6541. [[CrossRef](#)]
17. Tian, L.-L.; Li, S.-B.; Zhang, M.-J.; Li, S.-K.; Lin, L.-P.; Zheng, J.-X.; Zhuang, Q.-C.; Amine, K.; Pan, F. Cascading Boost Effect on the Capacity of Nitrogen-Doped Graphene Sheets for Li- and Na-Ion Batteries. *ACS Appl. Mater. Interfaces* **2016**, *8*, 26722–26729. [[CrossRef](#)]
18. Maulana, A.Y.; Futralan, C.M.; Kim, J. MOF-derived FeF_2 nanoparticles@graphitic carbon undergoing in situ phase transformation to FeF_3 as a superior sodium-ion cathode material. *J. Alloys Compd.* **2020**, *840*, 155719. [[CrossRef](#)]
19. Liang, Y.; Oettinger, J.D.; Zhang, P.; Xu, B. Ni or FeO nanocrystal-integrated hollow (solid) N-doped carbon nanospheres: Preparation, characterization and electrochemical properties. *Nanoscale* **2020**, *12*, 15157–15168. [[CrossRef](#)]
20. Xu, X.; Cao, R.; Jeong, S.; Cho, J. Spindle-like Mesoporous $\alpha\text{-Fe}_2\text{O}_3$ Anode Material Prepared from MOF Template for High-Rate Lithium Batteries. *Nano Lett.* **2012**, *12*, 4988–4991. [[CrossRef](#)]
21. Banerjee, A.; Singh, U.; Aravindan, V.; Srinivasan, M.; Ogale, S. Synthesis of CuO nanostructures from Cu-based metal organic framework (MOF-199) for application as anode for Li-ion batteries. *Nano Energy* **2013**, *2*, 1158–1163. [[CrossRef](#)]
22. Xuan, C.; Hou, B.; Xia, W.; Peng, Z.; Shen, T.; Xin, H.L.; Zhang, G.; Wang, D. From a ZIF-8 polyhedron to three-dimensional nitrogen doped hierarchical porous carbon: An efficient electrocatalyst for the oxygen reduction reaction. *J. Mater. Chem. A* **2018**, *6*, 10731–10739. [[CrossRef](#)]
23. Xue, S.; Yu, Y.; Wei, S.; Xu, B.; Lei, J.; Ban, R.; Wu, Q.-H.; Zheng, M.; Li, J.; Kang, J. Nitrogen-doped porous carbon derived from ZIF-8 as a support of electrocatalyst for enhanced oxygen reduction reaction in acidic solution. *J. Taiwan Inst. Chem. Eng.* **2018**, *91*, 539–547. [[CrossRef](#)]
24. Samuel, E.; Joshi, B.; Kim, M.-W.; Kim, Y.-I.; Park, S.; Kim, T.-G.; Swihart, M.T.; Yoon, W.Y.; Yoon, S.S. Zeolitic imidazolate framework-8 derived zinc oxide/ carbon nanofiber as freestanding electrodes for lithium storage in lithium-ion batteries. *J. Power Sources* **2018**, *395*, 349–357. [[CrossRef](#)]
25. Liu, X.; Liu, Y.; Feng, M.; Fan, L.-Z. MOF-derived and nitrogen-doped ZnSe polyhedra encapsulated by reduced graphene oxide as the anode for lithium and sodium storage. *J. Mater. Chem. A* **2018**, *6*, 23621–23627. [[CrossRef](#)]
26. Park, K.S.; Ni, Z.; Côté, A.P.; Choi, J.Y.; Huang, R.; Uribe-Romo, F.J.; Chae, H.K.; O’Keeffe, M.; Yaghi, O.M. Exceptional chemical and thermal stability of zeolitic imidazolate frameworks. *Proc. Natl. Acad. Sci. USA* **2006**, *103*, 10186–10191. [[CrossRef](#)]
27. Wang, Y.; Tian, W.; Wang, L.; Zhang, H.; Liu, J.; Peng, T.; Pan, L.; Wang, X.; Wu, M. A Tunable Molten-Salt Route for Scalable Synthesis of Ultrathin Amorphous Carbon Nanosheets as High-Performance Anode Materials for Lithium-Ion Batteries. *ACS Appl. Mater. Interfaces* **2018**, *10*, 5577–5585. [[CrossRef](#)]
28. Li, Y.; Hu, Y.-S.; Li, H.; Chen, L.; Huang, X. A superior low-cost amorphous carbon anode made from pitch and lignin for sodium-ion batteries. *J. Mater. Chem. A* **2015**, *4*, 96–104. [[CrossRef](#)]
29. Maulana, A.Y.; Song, J.; Lee, D.W.; Lee, C.E.; Kim, J. Enhanced electrochemical performance of graphitic carbon-wrapped spherical FeOF nanoparticles using maleopimaric acid as a cathode material for sodium-ion batteries. *J. Mater. Sci. Technol.* **2021**, *85*, 184–193. [[CrossRef](#)]
30. Swain, P.; Viji, M.; Mocherla, P.S.; Sudakar, C. Carbon coating on the current collector and LiFePO_4 nanoparticles—Influence of sp and sp-like disordered carbon on the electrochemical properties. *J. Power Sources* **2015**, *293*, 613–625. [[CrossRef](#)]
31. Tuinstra, F.; Koenig, J.L. Raman Spectrum of Graphite. *J. Chem. Phys.* **1970**, *53*, 1126–1130. [[CrossRef](#)]
32. Bin, D.-S.; Lin, X.-J.; Sun, Y.-G.; Xu, Y.-S.; Zhang, K.; Cao, A.-M.; Wan, L.-J. Engineering Hollow Carbon Architecture for High-Performance K-Ion Battery Anode. *J. Am. Chem. Soc.* **2018**, *140*, 7127–7134. [[CrossRef](#)]
33. Jae, W.; Song, J.; Hong, J.J.; Kim, J. Raspberry-like hollow Ni/NiO nanospheres anchored on graphitic carbon sheets as anode material for lithium-ion batteries. *J. Alloy. Compd.* **2019**, *805*, 957–966. [[CrossRef](#)]
34. Dou, P.; Cao, Z.; Wang, C.; Zheng, J.; Xu, X. Multilayer Zn-doped SnO_2 hollow nanospheres encapsulated in covalently interconnected three-dimensional graphene foams for high performance lithium-ion batteries. *Chem. Eng. J.* **2017**, *320*, 405–415. [[CrossRef](#)]

35. Yanuar, M.A.; Kim, J. FeOF nanoparticles wrapped by graphitic carbon layers prepared from Fe-MIL-88B as a cathode material for sodium-ion batteries. *Carbon* **2019**, *149*, 483–491. [[CrossRef](#)]
36. Zhang, X.; Fan, Q.; Yang, H.; Xiao, H.; Xiao, Y. Metal–organic framework assisted synthesis of nitrogen-doped hollow carbon materials for enhanced supercapacitor performance. *New J. Chem.* **2018**, *42*, 17389–17395. [[CrossRef](#)]
37. Wee, J.-H.; Kim, C.H.; Lee, H.-S.; Choi, G.B.; Kim, D.-W.; Yang, C.-M.; Kim, Y.A. Enriched Pyridinic Nitrogen Atoms at Nanoholes of Carbon Nanohorns for Efficient Oxygen Reduction. *Sci. Rep.* **2019**, *9*, 1–7. [[CrossRef](#)]
38. Liu, J.; Zhang, Y.; Zhang, L.; Xie, F.; Vasileff, A.; Qiao, S.Z. Graphitic carbon nitride (g-C₃N₄)-derived N-rich graphene with tuneable interlayer distance as a high-rate anode for sodium-ion batteries. *Adv. Mater.* **2019**, *31*, 1901261. [[CrossRef](#)] [[PubMed](#)]
39. Ye, G.; Zhu, X.; Chen, S.; Li, D.; Yin, Y.; Lu, Y.; Komarneni, S.; Yang, D. Nanoscale engineering of nitrogen-doped carbon nanofiber aerogels for enhanced lithium ion storage. *J. Mater. Chem. A* **2017**, *5*, 8247–8254. [[CrossRef](#)]
40. Agubra, V.A.; Fergus, J.W. The formation and stability of the solid electrolyte interface on the graphite anode. *J. Power Sources* **2014**, *268*, 153–162. [[CrossRef](#)]
41. Qiu, Z.; Lin, Y.; Xin, H.; Han, P.; Li, D.; Yang, B.; Li, P.; Ullah, S.; Fan, H.; Zhu, C.; et al. Ultrahigh level nitrogen/sulfur co-doped carbon as high performance anode materials for lithium-ion batteries. *Carbon* **2018**, *126*, 85–92. [[CrossRef](#)]
42. Song, J.; Kim, H.; Jae, W.; Kim, T.; Futralan, C.M.; Kim, J. Porous ZnO/C microspheres prepared with maleopimaric acid as an anode material for lithium-ion batteries. *Carbon* **2020**, *165*, 55–66. [[CrossRef](#)]